

Dynamics and kinetics of monolayer CH₄ on MgO(001) studied by helium-atom scattering

David R. Jung, Jinhe Cui, and Daniel R. Frankl

The Pennsylvania State University, University Park, Pennsylvania, 16802

(Received 29 August 1990; revised manuscript received 7 December 1990)

The structure, vibrational excitations, and adsorption and desorption kinetics of monolayer CH₄ on MgO have been investigated using several techniques of helium scattering. Structural information is presented in the form of high-order diffraction-peak intensities. A vibrational excitation of 7.5 meV measured by time-of-flight methods shows no dispersion. This excitation energy is used in an analysis of the Debye-Waller effect for the [00] and $[\bar{1}0]$ beams. Studies of adsorption and desorption rates exploiting the He-methane diffuse-scattering cross section indicate an island-growth mode and allow determination of the desorption activation energy. Differences between the low-coverage adsorption rates for adsorption on fresh versus previously exposed surfaces suggest that higher-binding-energy sites are present after the desorption of a methane monolayer.

INTRODUCTION

Elastic scattering of helium atoms is an excellent probe of adsorption kinetics,¹⁻⁵ while inelastic scattering can be used to detect low-energy sagittally polarized surface vibrations.^{6,7} We apply these techniques in a study of monolayer methane on MgO.

Whereas on the graphite basal plane a CH₄ monolayer forms a triangular lattice with the same symmetry and similar nearest-neighbor distance (4.26 Å) as found in bulk methane (4.2 Å), on the square lattice of MgO it forms a $c(2 \times 2)$ structure over a wide range of temperature and vapor pressure. This has been verified by low-energy electron diffraction,⁸ neutron scattering,^{9,10} and atom scattering.¹¹ Moreover, quasielastic neutron scattering¹² at 88 and 97 K, where the methane is in two-dimensional fluid state, has shown a low mobility compared with methane on graphite. Calculations employing sums of empirical pair potentials have indicated a rather large corrugation of the well depth on MgO (up to 30 meV or 20%),¹³ which, along with compatible $c(2 \times 2)$ lattice spacing on MgO (4.21 Å), enables the formation of the square structure.

Selective adsorption resonances in helium scattering from the methane monolayer have been analyzed to give the three lowest binding energies of the He-CH₄/MgO interaction potential.¹¹ A semiempirical calculation¹¹ of this potential which considered four possible orientations of the tetrahedral methane molecule [tripod, (110) dipod, (100) dipod, and free rotor] gave energies in fair agreement with experiment for the dipod and free rotor cases, but seemed to rule out the tripod configuration. Although this work could not uniquely determine the orientational state of the molecule in the temperature range of the experiment (22–41 K), Coulomb *et al.*⁹ claim some evidence, based on fits to neutron-scattering data taken at 2 and 10 K, for a (100) dipod orientation, while Deprick and Julg⁴ find support for either dipod orientation in a calculation of adsorption energies.

Of course, more information is contained in elastic

helium-scattering data than is usually extracted. If the exact potential were known, close-coupling scattering calculations (with correction for inelastic and instrumental effects) should yield line shapes consistent with experiment. The best agreement is found for cases in which both the adsorbate and substrate interaction parameters are relatively well known.^{15,16} A recent close-coupling calculation by Scoles *et al.* was compared with their He-scattering data from a HCl monolayer on graphite.¹⁷ The poor fit found using a free rotor configuration was taken as evidence for a preferred orientation of the nonspherical molecules in this system. An earlier study of CH₃F and CH₃Cl on bare and xenon-plated graphite by the same group used a comparison with a molecular-dynamics simulation to interpret the orientational ordering of the molecules, since the complexity of the molecules discouraged a close-coupling calculation.¹⁸

In the case of inelastic scattering from rare-gas monolayers or multilayers adsorbed on close-packed metal surfaces¹⁹⁻²¹ and on graphite,²² two types of behavior have been observed. First, the up-and-down vibrational mode is essentially dispersionless, i.e., an independent Einstein oscillator. Second, adsorbate-substrate coupling causes hybridization of this mode with the substrate Rayleigh mode where they have an avoided crossing.²³ Resonance of adsorbate and substrate vibrations is possible from this crossing point down to the center of the Brillouin zone, and in this region a lifetime broadening of about 0.5 meV was determined for Kr/Pt.²¹ There was essentially no difference between the dynamical behavior of the rare gases on Ag and Pt, while for Xe/Gr the data showed similar behavior, but did not yield quantitative comparison due to lower signal-to-noise ratio.

The results below concern primarily the dynamics and kinetics of methane on MgO, although additional structural information is also included in the form of diffraction beam intensities. Taken together with the earlier selective adsorption resonance measurements, these results provide a large data base for further theoretical analysis, such as close-coupling calculations, which will

require proper modeling of the interaction potentials, the methane orientation, and inelastic effects.

EXPERIMENT

Our apparatus employs two mass spectrometers for the detection of scattered helium beams. A quadrupole mass spectrometer (QMS) resides inside the scattering chamber with an entrance slit a distance 50 mm from the sample. It may be moved through any angle in the plane of incidence and translated about 5 cm perpendicular to this plane. A magnetic-sector mass spectrometer (MSMS) resides approximately 1 m from the sample in the last of four differentially pumped stages. Since it is fixed at an angle 90° to the incident beam, it can detect the specular beam at $\theta_i=45^\circ$, or, at other angles of incidence, diffraction and other beams with parallel momentum different from the specular (e.g., inelastic beams).

The signal from the QMS is collected in a current sensing mode, a lock-in amplifier referenced to the rotation of a 40% duty cycle chopper in the beam source being used to minimize noise. The lower helium background at the MSMS allows the detection of much weaker beams. This is done via the detection of individual pulses which are recorded in time by a multichannel analyzer (Nicolet No. 1170) over many cycles of the beam chopper. In this mode, a narrow duty cycle chopper is used, yielding for specular beams from the bare surface a time width of approximately 30 μ s. This width includes contributions from the chopper,²⁴ the length of the ionizing region, and the velocity spread of the beam. The latter is approximately 1% for the incident energy of 17.4 meV used here, as determined from the widths of diffraction beams from bare MgO,²⁵ and is also consistent with the nozzle diameter (7.5 μ m) and pressure [300 psi (gauge)].²⁶ For non-time-resolved detection with the MSMS, the signal is either integrated by the multichannel analyzer, or the current-sensing mode is used as with the QMS.

The background pressure (with the beam and QMS off) in the scattering chamber employing a cryopump (Air Products, Allentown, PA) was typically 2×10^{-10} torr. During measurements with the MSMS and QMS, pressures rose to roughly 1×10^{-9} and 5×10^{-10} torr, respectively. This pressure difference was due primarily to the use of a larger beam aperture for the time-of-flight experiments (1.0 mm) than for the others (0.33 mm). The sample holder allows rotation in both polar and azimuthal angles of incidence (θ_i and ϕ_i), heating to 800 K, and cooling to 22 K.¹¹ The temperature is measured by a calibrated Pt resistance thermometer in the copper block that holds the crystal. The MgO crystal (Spicer, Ltd., London) is cleaved *in situ* to provide a clean, well-ordered surface.¹¹ The methane film is grown by admitting research grade CH₄ gas (99.99% purity) through a UHV leak valve via a stainless-steel capillary aimed directly at the crystal from a distance of about 8 mm. The effective methane pressure near the crystal is roughly 30 times the pressure change measured by an ion gauge in the scattering chamber, according to estimates based either on the effusive flow of the gas from the dose tube, or on the time to deposit a monolayer at low surface temperatures. The

deposition of the methane monolayer has been described before.¹¹

RESULTS

Structure of the methane monolayer

We first present measurements made with the MSMS. In Fig. 1 are scans in the angle of incidence, θ_i , of specular and diffraction beams made in the non-time-resolved mode. The real-space lattice determined by the angular positions of these peaks is $(\sqrt{2} \times \sqrt{2})R45^\circ$ or $c(2 \times 2)$, with lattice constant 4.21 Å. The methane [11] peak is at the same angular position as the [10] peak of the substrate, etc. The relative intensities of these peaks (Table I) are related to the shape of the interaction potential, somewhat analogous to the shape of an optical grating. Perfect analogy is lost due to inelastic interactions, and to the z variation of the potential, which includes both a soft repulsive wall and an attractive well. For these reasons, and due to a large corrugation, these intensities could not be fitted using a hard wall model employing a simple sinusoidal corrugation.²⁷ (The same was true for measurements of specular and diffraction intensities made at

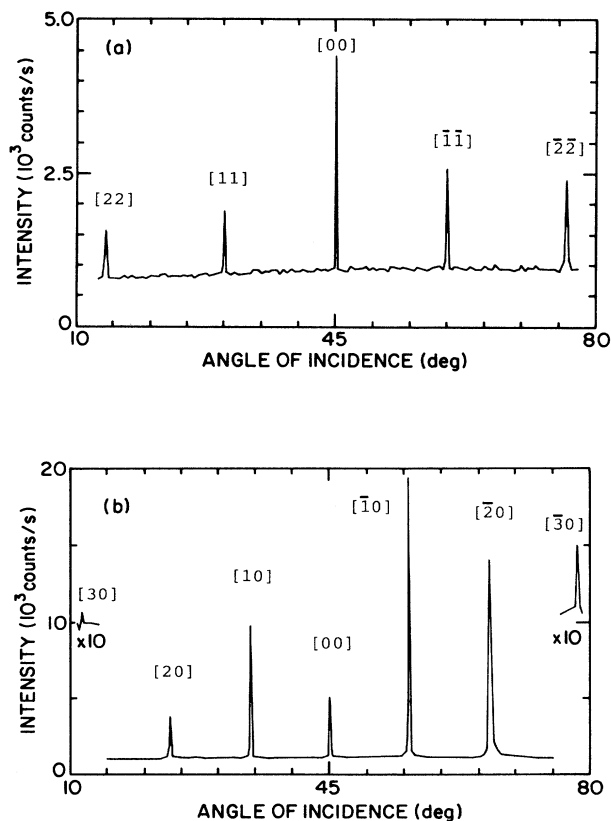


FIG. 1. Scans in θ_i along (a) the [11] and (b) the [10] directions of the methane lattice at temperatures of 33 and 36 K, respectively.

TABLE I. Normalized intensities, angular widths, and angles of incidence, of the overlayer diffraction peaks of Figs. 1(a) and 1(b). $I(G)$ is the overlayer peak intensity and I_S that of the substrate specular beam prior to deposition. Experimental uncertainties for the values of $I(G)/I_S(10^{-3})$, FWHM (deg), and θ_i (deg), are ± 0.02 , 0.05, and 0.05, respectively.

G	[22]	[11]	[00]	$[\bar{1}\bar{1}]$	$[\bar{2}\bar{2}]$
$I(G)/I_S(10^{-3})$	0.40	0.50	1.68	0.79	0.68
FWHM (deg)	0.26	0.18	0.18	0.17	0.37
θ_i (deg)	13.95	30.10	45.03	60.00	76.07

G	[30]	[20]	[10]	[00]	$[\bar{1}0]$	$[\bar{2}0]$	$[\bar{3}0]$
$I(G)/I_S(10^{-3})$	0.043	1.37	4.23	1.98	8.92	6.24	0.21
FWHM (deg)	0.28	0.23	0.15	0.17	0.21	0.31	0.34
θ_i (deg)	11.65	23.53	34.47	45.05	55.65	66.53	78.40

angles of incidence from 35° to 70° using the QMS.)

The observation of third-order peaks along the methane [10] azimuth, made possible by the high sensitivity of the MSMS, provides information on important higher Fourier components of the He-CH₄/MgO interaction that is not available from just the lowest order peaks. The large corrugation is especially evident along the methane [10] azimuth, where we see two oscillations in the diffraction-peak strength from left to right in the figure. Such an effect is known as “rainbow scattering” which, in the classical limit of short wavelength, gives maxima in the scattering intensity at two critical angles.²⁸ The large intensity of the $[\bar{1}0]$ beam is especially dramatic, being about 8 times greater than the corresponding first-order beam in the other azimuth, the $[\bar{1}\bar{1}]$ beam.

In Fig. 1 we also see asymmetry between pairs of peaks, with less intense diffraction for the more normal angle of incidence, especially along the [10] direction. This is evidence for inelastic effects in the scattering, since the inelastic coupling should be greater for θ_i near zero.⁶ Evidence that the asymmetry is not due to an instrumental effect is that the diffraction pattern from the bare MgO surfaces was fairly symmetrical,²⁵ as expected for purely elastic diffraction where, in this geometry, the beams are simply time reversals of each other. The broadening of the diffraction peaks over the specular peak is due to the scattering geometry and to the velocity spread of the beam. The specular peak [full width at half maximum (FWHM) $\approx 0.18^\circ$, Table I] is broadened over that of bare MgO [0.11° (Ref. 25)] due to disorder in the adsorbed layer.

Vibrational excitations

Time-of-flight data were taken at several angles in the two principal azimuths. These data were taken only from methane films grown immediately after a cleave (see “adsorption measurements” below). Sample spectra for the [11] and [10] azimuths are shown in Figs. 2(a) and 2(b). These were obtained over 2.0 and 2.5×10^6 pulses of the incident beam, respectively, using a channel width of 6 μ s, and at sample temperatures of 38 and 33 K. These and other spectra consistently show a broad region

(100–200 μ s wide) of enhanced signal on the creation side of the diffuse elastic peak E . Conservation of energy and momentum and the requirement $\theta_i + \theta_f = 90^\circ$ lead to the “scan curve” which describes the relationship between the energy $\hbar\omega$ and momentum $\Delta K = K_f - K_i$ of an inelastic feature:

$$\frac{\hbar\omega}{E_i} = \left[1 + \frac{\Delta K}{K_i} \right]^2 \tan^2 \theta_i - 1, \quad (1)$$

where K_i and K_f are the initial and final momenta parallel to the surface and E_i is the initial energy. The vibrational energies and momenta determined from measurements along the [11] direction and plotted in Fig. 2(c) show a mode with an energy of about 7.5 meV and with no significant dispersion. The polarization of this mode is assumed vertical, since the other possible sagittally polarized mode is longitudinal and would be more weakly coupled to the incident beam.⁷ The lack of dispersion suggests that for this mode the methane molecules behave as independent Einstein oscillators. The measured vibrational energy is significantly lower than that deduced in Ref. 11, 12 meV, based on the holding potential of Ref. 13 for methane on MgO. It is comparable to that of CH₄ on Cu(100), 6 meV, measured by atom scattering.² In the harmonic approximation, a 7.5 meV energy implies a force constant of 215 meV Å^{-2} for the methane-MgO potential.

The widths of the inelastic features observed here, estimated with some uncertainty due to the low signal-to-noise ratio to be 90 to 180 μ s, yield energy widths of 1.2–2.4 meV. Since the instrumental width at this flight time is negligible,²⁹ these measured widths are in fact due to surface vibrations. For Kr/Pt(111), there was no broadening of the mode when out of resonance, but near $\Gamma=0$ broadening of about 0.5 meV was clearly resolved.²¹ For Xe/Gr, we estimate broadening of order 1 meV based on the $\theta_i=41.5^\circ$ plot of Fig. 2 of Ref. 22. Mechanisms for broadening in the resonance regime²³ and nonresonance regime,³⁰ involve decay of the excitation via coupling to other modes. Multiphonon interactions are expected for these adsorbate systems based on the criterion of Goodman,³¹ i.e., since $E_i/\hbar\omega > 1$ (≈ 2).

However for a dispersionless mode, multiphonon excitations show up as higher harmonics, not broadening. The inelastic events represented by Fig. 2(b) for the [10] azimuth and Figs. 2(a) and 2(c) for the [11] azimuth all lie

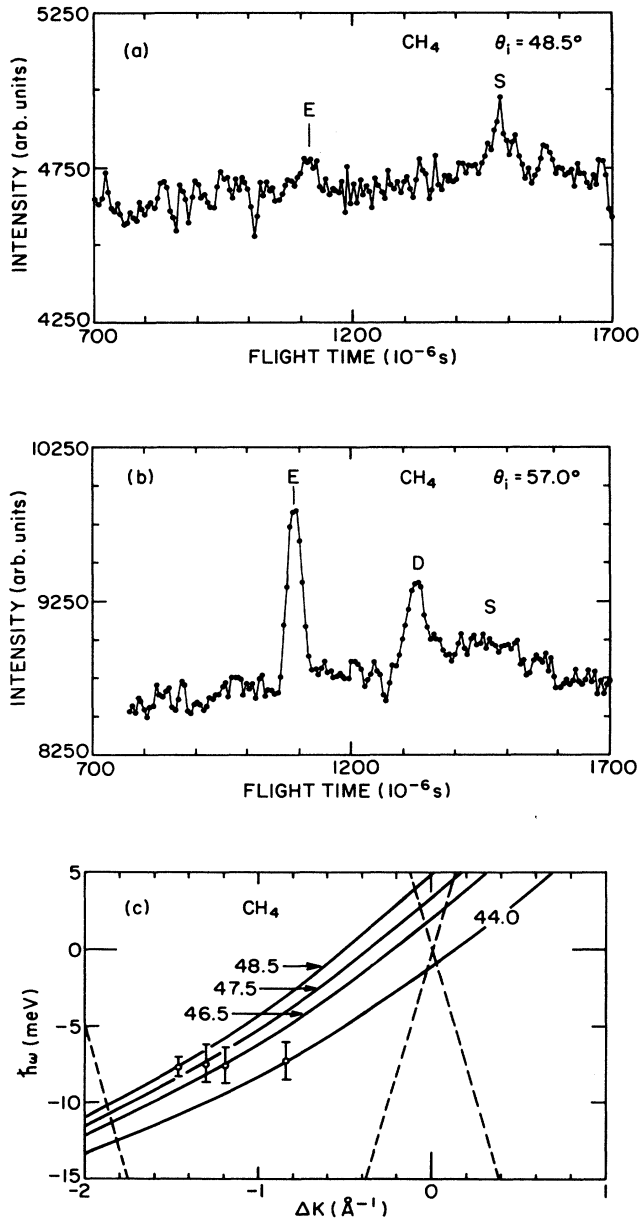


FIG. 2. Time-of-flight spectra (a) along the [11] and (b) the [10] directions of the methane lattice, showing phonon creation peaks, *S*, and elastic peaks, *E*. Peak *D* is the “deception” peak due to the elastic diffraction of a low-intensity wing of the velocity distribution of the incident beam (Ref. 37). (c) Dispersion plot along the [11] methane direction with energy error bars estimated from the widths of the peaks. Solid lines are scan curves for the corresponding angles of incidence. Dashed-dotted lines are the MgO surface Rayleigh mode.

at lower energy than the MgO surface Rayleigh mode (as well as the surface shear horizontal mode), and thus are not in resonance with any substrate mode. The enhanced broadening observed here may be due in part to coupling to low energy [≈ 1 meV (Ref. 32)] rotational modes of the methane molecules, that are not present in monatomic adsorbates. The absence of observable time-of-flight peaks corresponding to such excitations can be attributed to weak coupling.

Related to the direct measurement of vibrations by inelastic scattering is the measurement of the thermal attenuation of elastic scattering, the familiar Debye-Waller effect.³³ Figure 3 shows the intensities of both [00] and $[\bar{1}0]$ beams measured at $\theta_i = 70^\circ$ by the QMS detector as the surface was cooled and then warmed (to check for reversibility). To correct approximately for the decay in adlayer reflectivity due to aging of the surface, these intensities have been multiplied by a factor $\exp(t/\tau)$, where t is the time of the measurement after cleaving and where an attenuation time constant $\tau = 2 \times 10^4$ s has been fitted to the data. With this correction, there is very little difference between the intensities during cooling and warming, and the thermal attenuation of both beams is clearly evident.

Previous studies of thermal attenuation of elastic atom scattering indicate that, despite the inclusion of various correction factors, the phenomenon is not well understood.³³ In this light, we apply the usual Debye-Waller analysis more as a test of the model than for the determination of any physical quantities. The intensity of a diffraction beam *G* at a temperature *T* is assumed to follow

$$I_T(\mathbf{G}) = I_0(\mathbf{G}) \exp(-2W), \quad (2)$$

where the subscript 0 refers to the absence of thermal motion. The Debye-Waller factor is

$$2W = \langle (\Delta \mathbf{k} \cdot \mathbf{u})^2 \rangle = \Delta k_z^2 \langle u_z^2 \rangle + \Delta k_x^2 \langle u_x^2 \rangle, \quad (3)$$

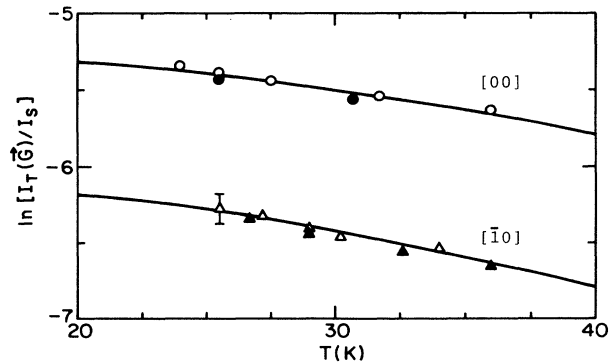


FIG. 3. Thermal attenuation of [00] and $[\bar{1}0]$ beams for $\theta_i = 70^\circ$ showing measurements during cooling (open symbols) and warming (solid symbols) with best fits of Eq. (6) (solid lines), as explained in text. The error bar for the specular beam data roughly equals the symbol size.

where $\Delta \mathbf{k}$ is the change in momentum of the He atom and \mathbf{u} is the vibrational displacement of an adsorbed CH_4 molecule. The momentum transfer perpendicular to the surface is given by

$$\Delta k_z = k_i [(\cos^2 \theta_i + D/E_i)^{1/2} + (\cos^2 \theta_f + D/E_i)^{1/2}] \equiv k_i A(\theta_i, \theta_f, D), \quad (4)$$

where $\theta_i = 70^\circ$ is the initial angle and $\theta_f = 70^\circ$ and 43° are the final angles (for the specular and diffraction beams of Fig. 3, respectively), E_i is the energy of the beam, and D is the well depth of the He- CH_4/MgO potential. For the first-order diffraction beam the momentum transfer parallel to the surface is simply $\Delta k_x = G = 1.49 \text{ \AA}^{-1}$. The inclusion of the well depth term, the ‘‘Beeby correction,’’³⁴ accounts for the classical acceleration of the atom by the interaction potential. The vertical surface vibration is modeled as harmonic and dispersionless, i.e., by Einstein oscillators of energy $\hbar\omega$ and mass M , for which³⁵

$$\langle u_z^2 \rangle = \left[\frac{\hbar}{2M\omega} \right] \coth \left[\frac{\hbar\omega}{2k_B T_s} \right]. \quad (5)$$

We assume the same form for the parallel vibrational amplitude, $\langle u_x^2 \rangle$, but with a different vibrational energy $\hbar\Omega$.

For actual comparison with our data, we use relative intensities $I_T(\mathbf{G})/I_S$ and $I_0(\mathbf{G})/I_S$ in Eq. (2), where I_S is the substrate specular intensity measured prior to monolayer deposition. Thus,

$$\ln \frac{I_T(\mathbf{G})}{I_S} = \ln \frac{I_0(\mathbf{G})}{I_S} - \left[\frac{\hbar k_i^2}{2M\omega} A^2(\theta_i, \theta_f, D) \coth \frac{\hbar\omega}{2k_B T} + \frac{\hbar G^2}{2M\Omega} \coth \frac{\hbar\Omega}{2k_B T} \right]. \quad (6)$$

For the specular beam, G and third term in Eq. (6) are zero. Assuming $\hbar\omega = 7.5 \text{ meV}$ from the time-of-flight results, the best fit is found with $D = 13.2 \pm 2 \text{ meV}$ and $\ln I_0[00]/I_S = -3.2 \pm 0.3$. For the diffraction beam, the third term in the equation is not zero, but it is about 60 times smaller than the second term (as long as $\hbar\Omega$ is of order or greater than $\hbar\omega$). If we neglect this term and assume as before $\hbar\omega = 7.5 \text{ meV}$, then a fit to the diffraction beam data yields $D = 14.5 \pm 2 \text{ meV}$ and $\ln I_0[\bar{1}0]/I_S = -3.5 \pm 0.3$. Thus, these fits to the specular and diffraction beam data, respectively, have been plotted in Fig. 3. It is encouraging that the two best-fitted well depths are nearly the same. The larger well depth for the diffraction beam may be due in part to the neglect of the third term of Eq. (6) or merely to experimental uncertainty, as these are of the same magnitude.

Based on selective adsorption measurements which placed the ground state at 3.6 meV and a semiempirical calculation which gave a well depth of about 6 meV,¹¹ these ‘‘Beeby’’ well-depth values are clearly larger than the true well depth. For the specular beam data, the fitted well depth can be lowered to 6 meV only if $\hbar\omega$ is

shifted to an unreasonably low value of about 1.5 meV. However, our results are qualitatively similar to those of Gibson and Sibener¹⁶ who found that the fitted well depth is larger at large angles of incidence.

Adsorption measurements

In this section we exploit the well-known sensitivity of the He elastic beam intensities to low coverages of adsorbates or defects. These measurements allow us to estimate the average methane diffuse-scattering cross section, to calibrate specular intensity dependence on coverage, and to study desorption rates as a function of temperature and coverage. The data have been taken at $\theta_i = 70^\circ$ using the QMS.

As shown in our previous paper,¹¹ the specular intensity from the methane monolayer is only about 3% of that from the bare surface. Therefore, the molecules are essentially diffuse scatterers which act to block the substrate. A series of azimuthal scans at partial coverages, made by intermittent dosing at 33 K, shown in Fig. 4, confirms that coherent scattering characteristic of the bare surface (i.e., showing substrate selective adsorption structures¹¹) dominates the specular intensity up to very high coverage. The zero coverage scan (a) shows two sharp minima due to the 0,(0,1) He-MgO resonance. The overlayer pattern does not dominate until $I/I_S \approx 10\%$ in scan (c). At $I/I_S = 6\%$ in scan (d), the substrate features are not seen at all, indicating complete blocking by the methane layer. There appears to be a minimum due to

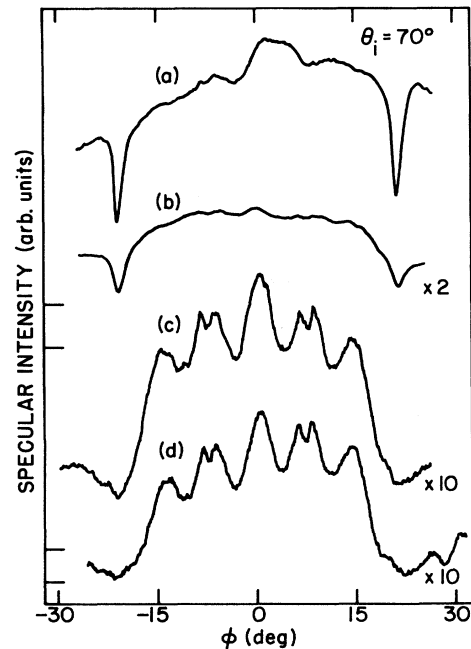


FIG. 4. Azimuthal scans at partial CH_4 coverage: $I/I_S = 1, 0.3, 0.1,$ and 0.06 , for curves (a)–(d). Scale factors and zero-level ticks are indicated to the right and left, respectively, of each scan. $\theta_i = 70^\circ$.

the substrate at about $\phi=20^\circ$, but this is actually due to the overlayer, as scans at other polar angles clearly showed the disappearance of substrate features on reaching this coverage.

The diffuse-scattering cross section σ is the surface area affected per molecule.³ At low coverages it may be quite large due to the long range of the Van der Waals attraction,³⁶ but at monolayer completion (assuming just one phase on the surface) it equals the area of the monolayer primitive unit cell. During the formation of the monolayer, each adsorbed molecule adds an effective diffuse-scattering cross section to the already diffusely scattering area of the surface. This causes the decrease of the specular intensity as a function of time. In the case of CO on Pt(111), the cross section at low coverage was found to be similar to that of gas phase CO ($\geq 250 \text{ \AA}^2$), leading to the conclusion that the CO molecules were widely spaced on the surface.³

The growth of the CH₄ monolayer has been studied at impingement rates of $1-(10 \times 10^{-3}) \text{ L s}^{-1}$ [1 langmuir (L) = 10^{-6} torr s] and in the temperature range 22 to 45 K. Figure 5 shows the intensity measured as the temperature was allowed to fall at a rate of 0.5 K/min. The two steep drops indicate the condensation of the first and second layers.

Measurements of the specular beam attenuation at constant temperature, which we shall call specular adsorption curves, are shown in Fig. 6. This is a series of six consecutive runs made at different temperatures but the same impingement rate. Curve (a) was taken 15 min after the cleave and successive curves were taken at approximately 15 min intervals thereafter. Between runs the surface was rapidly heated to about 80 K, and then allowed to cool and stabilize to the desired surface temperature. Curve (a) shows an attenuation that is quite linear all the way from zero to nearly fully monolayer coverage. This indicates that the scattering cross section is constant from beginning to end, which suggests that

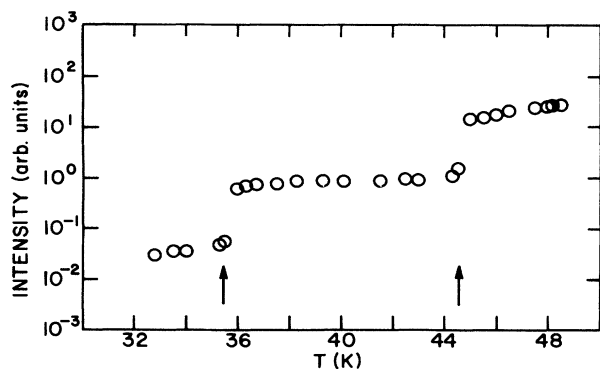


FIG. 5. First- and second-layer adsorption. The specular intensity as a function of temperature as methane is adsorbed at constant pressure. The condensation temperatures of the first and second layers are near $T=45$ and 36 K, respectively. The impingement rate is 0.008 L s^{-1} and $\theta_i=70^\circ$.

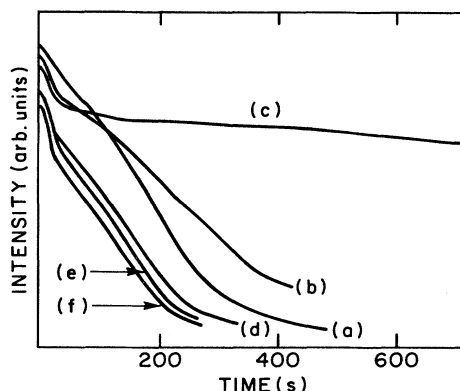


FIG. 6. Specular beam adsorption curves at different temperatures. Labels (a)–(f) denote the sequence of measurements taken at temperatures of 40.8, 41.5, 42.5, 40.5, 38.7, and 36.0 K, respectively. The impingement rate is 0.0033 L s^{-1} and $\theta_i=70^\circ$.

the layer grows by the addition of adsorbate molecules at the edges of islands. (This picture is consistent with the evidence shown in Fig. 4 for bare surface areas even at high methane coverage.) The density within the islands must be the same as of the full monolayer, which shows $c(2 \times 2)$ diffraction peaks. Due to its linearity, curve (a) allows a straightforward calibration of the methane impingement rate, which is fixed by the gas manifold pressure and the leak valve opening. The impingement rate is

$$J = \frac{1}{t_m \sigma_m S} = \frac{1}{t_m \sigma_m}, \quad (7)$$

where t_m is the monolayer completion time, $\sigma_m \approx 18 \text{ \AA}^2$ is the area of the monolayer primitive unit cell, and where a sticking coefficient, S , of 1 is assumed at the low temperatures of interest here. This yields $J=0.0033 \text{ L s}^{-1}$ for curve (a) of Fig. 5.

The other adsorption curves, taken after curve (a) (hence on a surface previously covered by methane) show two stages, each of a quite constant slope. In particular we may compare curve (a) with curve (d) taken at nearly the same temperature. In curve (d), the first stage is about twice as steep as the second. The second stage slope is approximately the same as that of the adsorption run on the virgin surface, curve (a). The second stage of curve (d) thus exhibits a diffuse-scattering cross section of about 18 \AA^2 , hence, assuming no difference in the sticking coefficient, the cross section for the first stage must be about 36 \AA^2 . The greater cross section of the first stage implies a lesser degree of overlap of each individual cross section with its neighboring diffuse scatterers. The same behavior, a nearly straight first adsorption curve followed by later curves which show two fairly

linear stages, was reproducible in other series of runs made at a single low temperature.

In addition we made the following observations coincident with the observation of two-stage adsorption behavior. First, the bare surface intensity decayed during the measurements of Fig. 6 with a time constant of about 7 h, while the time required to reach the plateau of the attenuation curve decreased as well. Since the onset of attenuation does correspond—with only a slight reproducible delay—to the onset of gas dosing, this implies that the methane fluence required to reach the plateau decreases and hence that the nondiffusively scattering surface area present between successive runs also decreases. Second, the duration of the first stage, which is typically 10% of the monolayer exposure time and is constant for a given series of runs, was found to vary slightly from cleave to cleave. Third, simply allowing the surface to age prior to the first deposition does not produce the two-stage behavior. One series of curves was taken on a surface which was allowed to age 90 min in a poor background pressure (5×10^{-10} torr) prior to the start of the first run. Again, the first curve showed only a slight change in slope, while the second curve showed the usual factor-of-2 change. This suggests that exposure to methane alters the surface in a way different from exposure to ambient gases.

To investigate the nature of the two-stage adsorption further, the $[\bar{1}0]$ diffraction peak was monitored during adsorption on a surface previously exposed to methane at $T < 41$ K (Fig. 7). The diffraction peak shows no intensity until after the onset of the second stage of the specular curve. Thus, the first stage does not have the $c(2 \times 2)$ structure.

The temperature and pressure dependence of the specular adsorption curves may be summarized as follows.

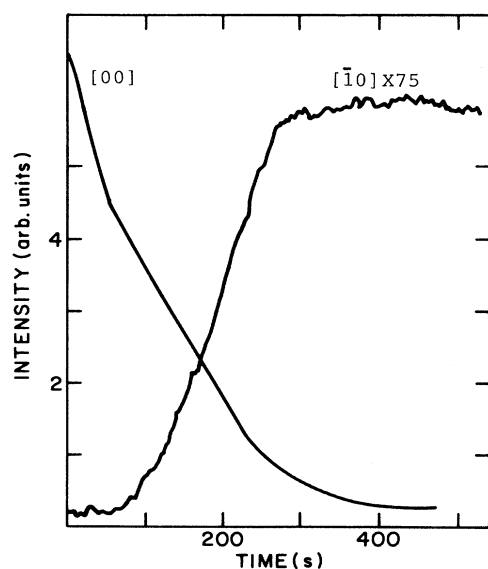


FIG. 7. Adsorption curves for $[00]$ and $[\bar{1}0]$ beams, with $\theta_i = 70^\circ$ and an impingement rate of 0.0036 L s^{-1} .

At temperatures of $22 < T < 38$ K and impingement rates less than 0.01 L s^{-1} , the shape and slope of the specular adsorption curve was found to be independent of surface temperature, and the second stage slope was found to be proportional to impingement rate. This suggests that in this temperature range the sticking coefficient is virtually constant and that the molecules rapidly move to the islands upon arrival on the surface. Above 40 K, the second-stage slope decreases rapidly with increasing temperature. For the curve (e), (d), (b), and (c) of Fig. 6, the second-stage slopes at temperatures of 38.7, 40.5, 41.5, and 42.5 K, respectively, were 2.8, 2.6, 1.7, and $0.5 \times 10^{-3} \text{ s}^{-1}$.

The specular intensities attained after desorption of a film depended on how much, if at all, the surface was heated. The intensity following desorption without heating ($T \leq 42$ K) was usually less than that attained if the temperature was raised to ≈ 80 K but more than the intensity at the break point in the preceding run. The increase in intensity on heating from 42 to 80 K was, however, sometimes not observed, particularly on surfaces, several hours old. Due to the apparent sensitivity of the result to several factors including the quality of the initial cleave, the ambient bare pressure, and the number of exposures to methane, the question of this more strongly bound phase was not investigated further.

Desorption measurements

Desorption has been studied at constant temperature by simply stopping the CH_4 gas exposure after monolayer coverage has been reached and monitoring the rise of the He specular intensity over time. These desorption curves show virtually constant slope at high coverages (above 60%). In this regime, this suggests (1) constant diffuse-scattering cross section per desorbing molecule, hence (2) desorption from island edges, and (3) a desorption rate that is virtually coverage independent. This is consistent with a zeroth-order desorption process and is similar to the result of Gibson and Sibener for the desorption of Xe from $\text{Ag}(111)$.²⁰ The general form of rate equation for desorption is

$$\frac{d\theta}{dt} = -\nu^n \theta^n \exp(-E_d/kT), \quad (8)$$

where the “attempt frequency” ν and the desorption activation energy E_d are assumed to depend only weakly on θ and T , and where n is the order of the desorption process. In Fig. 8, an Arrhenius plot shows a fair linear least-squares fit to the desorption rates taken in the high-coverage regime. The best-fitted slope gives an activation energy of 136 meV (independent of the assumed rate order n), in good agreement with the heat of adsorption (137 meV) measured at monolayer coverage by the volumetric isotherm method.¹⁰ The best-fit intercept is 2.9×10^{15} . The exponential dependence of the desorption rate on temperature accounts for the temperature dependence of the second-stage slopes in Fig. 6.

Discussion of kinetics results

The linearity of the specular adsorption curves and the persistence up to high coverages of the bare surface selec-

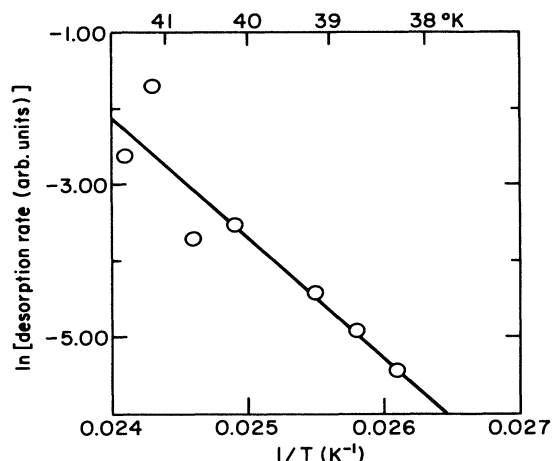


FIG. 8. Arrhenius plot of \ln (desorption rate) vs $(1/T)$ (K^{-1}). Desorption rate are in units of intensity (arbitrary units) per second. Rates taken in a high-coverage regime (above 60% where the desorption curves were linear). Slope of the fitted equivalent to 136 meV.

tive adsorption pattern show that the methane monolayer on MgO forms by the growth of islands. Desorption from the high-coverage film apparently proceeds by the removal of molecules from island edges, as well. The temperature dependence of the desorption curves made at high coverages shows an activation energy which is consistent with the known monolayer heat of adsorption.

Interesting two-stage adsorption curves are observed during adsorption on previously exposed surfaces. The adsorption in the first stage is disordered and characterized by a diffuse-scattering cross section roughly double that in the second, island-growth stage. [The first stage cannot be due to a gas phase on the surface since (1) the diffuse-scattering cross section for gas-phase adsorbates is typically 100–200 Å (Ref. 13) and (2) there would then be a temperature dependence of the coverage at which the break in slope occurs which would delineate the gas-solid phase boundary.] The binding energies at these first-stage adsorption sites must be higher than at the sites where the $c(2 \times 2)$ phase grows, since only when these sites are filled does island growth begin. The higher diffuse-scattering cross section in the first stage is still only one-third of the gas-phase He-CH₄ cross section,³⁸ hence the first stage involves the overlap of the gas-phase

methane cross sections with those of other diffuse scatterers. This and the correlation of the observation of two-stage behavior with methane exposure and decay of the bare surface reflectivity, link the first-stage adsorption to the presence of some kind of defect, whose identity we have not determined. These defects sites are apparently different from any defect sites present on the freshly cleaved surface, since the latter do not result in two-stage adsorption behavior. It is interesting to note that even though the area of the $c(2 \times 2)$ phase shrinks with successive depositions and increasing surface age, the amount of methane adsorbing in the “first stage” on each deposition remains roughly constant.

SUMMARY

In this paper, structural, dynamical, and kinetic information has been presented from analysis of elastic and inelastic helium scattering from monolayer CH₄/MgO. Diffraction-peak intensities observed out to third order give evidence for large corrugation and inelastic effects in the He-CH₄/MgO interaction. An Einstein-like vibrational mode with energy about 7.5 meV has been found in time-of-flight spectra. The thermal attenuation of the [00] and [10] beams is fitted by a Debye-Waller model using the interaction potential well depth in the Beeby correction. For a harmonic vibrational energy of 7.5 meV, the specular beam data are fitted well with a well depth of 13.2 ± 2 MeV, but this is not consistent with the interaction potentials of Ref. 11. The fit to the diffraction beam data neglecting lateral adsorbate motion yields a slightly larger well depth. Evidence for island growth of the methane monolayer was found in measurements of the adsorption rate during constant, isothermal dosing. Desorption rates measured by cutting off dosing suggest a desorption activation energy quite similar to the known monolayer heat of adsorption. Differences between the low-coverage adsorption rates for adsorption on fresh versus previously exposed surfaces suggests that higher-binding-energy sites are present after the desorption of a methane monolayer.

ACKNOWLEDGMENTS

We thank Professor M. W. Cole for helpful discussions and Mr. X. Liang for assistance with part of the data collection and analysis. This work was supported by the National Science Foundation under Grant No. DMR-8718771.

¹B. F. Mason, R. Caudano, and B. R. Williams, *Phys. Rev. Lett.* **47**, 1141 (1981).

²B. F. Mason, R. Caudano, and B. R. Williams, *J. Chem. Phys.* **77**, 562 (1982).

³Bene Poelsema, Laurens K. Verheij, and George Comsa, *Phys. Rev. Lett.* **49**, 578 (1982); **49**, 1731 (1982).

⁴Bene Poelsema, Laurens K. Verheij, and George Comsa, *Phys. Rev. Lett.* **51**, 2410 (1983).

⁵J. Lapujoulade, Y. Le Cruer, M. Lefort, Y. Lejay, and E.

Maurel, *Surf. Sc.* **118**, 103 (1982).

⁶J. P. Toennies, *Phonon Interactions in Atom Scattering from Surfaces*, in *Dynamics of Gas-Surface Interactions*, edited by G. Benedek and U. Valbusa (Springer, Berlin, 1982).

⁷V. Celli and D. Eichenauer, in *Proceedings of the Second International Conference on Phonon Physics, Budapest, 1985*, edited by J. Kollar *et al.* (World Scientific, Singapore, 1985), p. 612.

⁸T. Meichel, J. Suzanne, and J.-M. Gay, *C.R. Acad. Sci. (Paris)*

- 303, 989 (1986).
- ⁹J. P. Coulomb, K. Madih, B. Croset, and H. J. Lauter, *Phys. Rev. Lett.* **54**, 1536 (1985).
- ¹⁰K. Madih, Ph.D. thesis, Universite D'Aix-Marseille, 1986.
- ¹¹D. R. Jung, J. Cui, D. R. Frankl, G. Ihm, H.-Y. Kim, and M. W. Cole, *Phys. Rev. B* **40**, 11 893 (1989).
- ¹²M. Bienfait, J. P. Coulomb, and J. P. Palmari, *Surf. Sci.* **182**, 557 (1987).
- ¹³C. Girard and C. Girardet, *Chem. Phys. Lett.* **138**, 83 (1987).
- ¹⁴B. Deprick and A. Julg, *New J. Chem.* **11**, 299 (1987).
- ¹⁵J. M. Huston and C. Schwartz, *J. Chem. Phys.* **79**, 5179 (1983).
- ¹⁶K. D. Gibson, C. Cerjan, J. C. Light, and S. J. Sibener, *J. Chem. Phys.* **88**, 7911 (1988).
- ¹⁷G. Y. Liu, P. Rowntree, G. Scoles, and J. Xu, *Surf. Sci.* **224**, 43 (1989).
- ¹⁸J. C. Ruiz-Suarez, M. L. Klein, M. A. Moller, P. A. Rountree, G. Scoles, and J. Xu, *Phys. Rev. Lett.* **61**, 710 (1988).
- ¹⁹B. F. Mason and B. R. Williams, *Phys. Rev. Lett.* **46**, 1138 (1981).
- ²⁰K. D. Gibson and S. J. Sibener, *Faraday Discuss. Chem. Soc.* **80**, 023 (1985); *J. Chem. Phys.* **88**, 7862 (1988).
- ²¹K. Kern, P. Zeppenfeld, R. David, and G. Comsa, *Phys. Rev. B* **35**, 886 (1987); *J. Electron. Spectrosc. Relat. Phenom.* **44**, 215 (1987).
- ²²J. P. Toennies and R. Vollmer, *Phys. Rev. B* **40**, 3495 (1989).
- ²³B. Hall, D. L. Mills, and J. E. Black, *Phys. Rev. B* **32**, 4932 (1985).
- ²⁴B. D. Weaver and D. R. Frankl, *Rev. Sci. Instrum.* **59**, 92 (1988).
- ²⁵J. Cui, D. R. Jung, and D. R. Frankl, *Phys. Rev. B* **42**, 9701 (1990).
- ²⁶B. D. Weaver and D. R. Frankl, *Rev. Sci. Instrum.* **58**, 2115 (1987).
- ²⁷U. Garibaldo, A. C. Levi, R. Spadacini, G. E. Tommei, *Surf. Sci.* **48**, 649 (1975).
- ²⁸J. D. McClure, *J. Chem. Phys.* **52**, 2712 (1970).
- ²⁹Two competing effects determine the instrumental energy resolution as a function of final energy. (1) $\delta E/\delta t$ goes to zero with increasing flight time, t , and (2) the instrumental time width due to the velocity spread of the beam becomes larger with increasing flight time. The former effect dominates, so that the resolution of our instrument, which is about 1 meV at the elastic peak (17.4 meV), becomes about 0.5 meV at a final energy of 10 meV.
- ³⁰J. C. Ariyasu, D. L. Mills, K. G. Lloyd, and J. C. Hemminger, *Phys. Rev. B* **30**, 507 (1984).
- ³¹F. O. Goodman, *Surf. Sci.* **26**, 327 (1971).
- ³²G. Herzberg, *Infra-red and Raman Spectra of Polyatomic Molecules* (Van Nostrand, New York, 1945).
- ³³T. Engel and K. H. Rieder, in *Structural Studies of Surfaces*, Springer Tracts in Modern Physics, Vol. 91 (Springer, Berlin, 1982).
- ³⁴J. L. Beeby, *J. Phys. C* **4**, L359 (1971).
- ³⁵N. W. Ashcroft and N. D. Mermin, *Solid State Physics* (Saunders College, Philadelphia, 1976).
- ³⁶H. Jonsson, J. H. Weare, and A. C. Levi, *Surf. Sci.* **148**, 126 (1984).
- ³⁷W. Allison, R. F. Willis, and M. Cardillo, *Phys. Rev. B* **23**, 6824 (1981).
- ³⁸U. Buck, K. H. Kohl, A. Kohlhase, and M. Faubel, *Mol. Phys.* **55**, 1255 (1985).